7-2018

Effects of Nb and Ta additions on the strength and coarsening resistance of precipitation-strengthened Al-Zr-Sc-Er-Si alloys

Dinc Erdeniz
Marquette University, dinc.erdeniz@marquette.edu

Anthony De Luca
Northwestern University

David N. Seidman
Northwestern University

David C. Dunand
Northwestern University

Materials Characterization, Vol. 141 (July 2018): 260-266. DOI.

Effects of Nb and Ta additions on the strength and coarsening resistance of precipitation-strengthened Al-Zr-Sc-Er-Si alloys

Dinc Erdeniz
Department of Materials Science and Engineering, Northwestern University, Evanston, IL
Anthony De Luca
Department of Materials Science and Engineering, Northwestern University, Evanston, IL
Northwestern University Center for Atom Probe Tomography, Northwestern University, Evanston, IL
David N. Seidman
Department of Materials Science and Engineering, Northwestern University, Evanston, IL
Northwestern University Center for Atom Probe Tomography, Northwestern University, Evanston, IL
NanoAl LLC, 8025 Lamon Avenue, Skokie, IL
David C. Dunand
Department of Materials Science and Engineering, Northwestern University, Evanston, IL
NanoAl LLC, 8025 Lamon Avenue, Skokie, IL

Abstract

A dilute Al-0.07Zr-0.02Sc-0.005Er-0.06Si (at.%) alloy was microalloyed with 0.08 at.% Nb or Ta. Atom-probe tomography reveals that, upon aging, Nb and Ta partition to the coherent $L1_2$-Al_3(Zr,Sc,Er) nanoprecipitates (with average concentrations of 0.2 and 0.08 at.%, respectively), with both segregating at the matrix/nanoprecipitate heterophase interface. This is consistent with the Nb- and Ta-modified alloys exhibiting, as compared to the unmodified alloy: (i) higher peak microhardness, from a higher nanoprecipitate volume fraction and/or lattice parameter mismatch; and (ii) improved aging resistance, from slower nanoprecipitate coarsening due to the small diffusivities of niobium and tantalum in aluminum. Analogous results were previously reported for a V-modified alloy.

Keywords

Aluminum alloys, Precipitation strengthening, Coarsening, Microhardness, Atom-probe tomography

1. Introduction

Within the last few decades, much research has focused on aluminum micro-alloyed with scandium, which can be aged to create coherent, $L1_2$-ordered tri-aluminide nanoprecipitates (Al_3Sc), which are coarsening-resistant up to 300 °C and which interact efficiently with matrix dislocations, thereby increasing the ambient strength and creep resistance of the alloys [[1], [2], [3], [4], [5], [6], [7], [8], [9], [10], [11]].

Recent research has focused on identifying additional alloying elements, which can partially (or fully) replace the rather expensive scandium, while maintaining the $L1_2$ structure of the nanoprecipitates and also: (i) increasing creep resistance, by increasing the lattice parameter mismatch between the nanoprecipitates and matrix (e.g. lanthanides [[12], [13], [14], [15], [16], [17], [18], [19], [20], [21]]) and thus increase the resistance by nanoprecipitates to the movement of the matrix's dislocations; and/or (ii) improving the precipitate coarsening resistance through their small diffusivities in the matrix (e.g., transition metals [[22], [23], [24], [25], [26], [27], [28], [29], [30], [31], [32], [33]]), so these alloys can be used well above 300 °C. Ideally, an alloying addition would satisfy both these conditions. However, an element increasing the precipitate lattice parameter mismatch, while improving creep resistance of the alloy, may also increase the driving force for coarsening. Therefore, a compromise between creep and coarsening resistance is often necessary, and two (or more) elements can be used, one increasing lattice parameter mismatch and the other displaying small diffusivity in the aluminum matrix. To date the elements erbium and zirconium have produced the best results as additions to Al-Sc alloys, because they very effectively: (i) increase the number density of nanoprecipitates and increase the lattice parameter mismatch and thereby the creep resistance (for Er); and (ii) significantly reduce the nanoprecipitate coarsening kinetics (for Zr), thus allowing the use of these alloys at higher temperatures [17,34]. Furthermore, additions of silicon, which act as inoculants, result in Al-Sc-Zr-Er-Si alloys that have high microhardness values upon peak-aging and are coarsening- and creep-resistant at temperatures up to 400 °C [35].

To further increase coarsening resistance, Zr and Sc can be partially replaced by transition metals with even smaller diffusivities in Al [24]. Earlier research [23] showed that Group 5 transition elements (G5 = V, Nb or Ta), all of which have much smaller diffusivities in aluminum than Zr and Sc, partition to the $L1_2$ Al_3(Sc,G5) nanoprecipitates in small concentrations (<3 at.%). In our previous work [36], we studied the effects of vanadium on coarsening- and creep-resistance of a castable Al-Er-Sc-Zr-Si alloy labeled Q2 (Table 1); V additions increased the coarsening resistance of the alloy, while the creep resistance remained unaffected. In a recent study [37], the three Group 5 (G5) transition metals (V, Nb and Ta) were added individually into arc-melted Al-Er-Sc-Zr alloys; these alloys were Sc-rich and Zr-poor, unlike the alloys Q2, Q4 and Q5 (with V, Nb and Ta, Table 1) studied herein, which are Zr-rich and Sc-poor. That study [37] revealed that vanadium decreased the

coarsening kinetics during isochronal aging, whereas niobium and tantalum had no noticeable effects. Atom-probe tomography (APT) [38,39] results demonstrated that only V partitioned significantly to the precipitates (~2.75 at.%).

Table 1. Average concentrations (at.%) of all atom-probe tomographic (APT) nanotips analyzed for this study, compared to concentrations measured by direct current plasma-atomic emission spectrometry (DCP-AES) on macroscopic volumes. Data for alloys Q1 and Q2 are from Ref. [36] (Nom = Nominal, ND = not detected).

	Er	Sc	Zr	V	Nb	Ta	Si	$L1_2$ Formers*	Technique
Q1-Nom	0.005	0.02	0.07	–	–	–	0.06	0.095	
Q1	0.005	0.019	0.068	–	–	–	0.066	0.092	DCP-AES
Q2-Nom	0.005	0.02	0.07	0.08	–	–	0.06	0.175	
Q2	0.007	0.013	0.071	0.074	–	–	0.054	0.165	DCP-AES
Q4-Nom	0.005	0.02	0.07	–	0.08	–	0.06	0.175	
Q4	0.006	0.007	0.071	–	0.047	–	0.054	0.131	DCP-AES
Q4-1	0.004	0.009	0.242	–	0.157	–	0.057	0.412	APT
Q4-2	0.006	0.014	0.355	–	0.024	–	0.053	0.399	APT
Q4-3	ND	ND	0.205	–	0.176	–	0.064	0.381	APT
Q4-4	ND	0.018	0.117	–	0.083	–	0.077	0.218	APT
Q4-5	0.015	0.064	0.337	–	0.154	–	0.119	0.570	APT
Q4-6	0.001	0.002	0.100	–	0.020	–	0.075	0.123	APT
Q4-7	ND	0.002	0.108	–	0.210	–	0.055	0.320	APT
Q4-8	0.004	0.003	0.146	–	0.055	–	0.075	0.208	APT
Q4-Ave	0.006 ± 0.005	0.016 ± 0.022	0.201 ± 0.102	–	0.110 ± 0.073	–	0.072 ± 0.021	0.329 ± 0.142	
Q5-Nom	0.005	0.02	0.07	–	–	0.08	0.06	0.175	
Q5	0.006	0.009	0.074	–	–	0.052	0.082	0.141	DCP-AES
Q5-1	0.002	0.026	0.251	–	–	0.063	0.073	0.339	APT
Q5-2	ND	0.030	0.171	–	–	0.065	0.077	0.266	APT
Q5-3	0.002	0.006	0.149	–	–	0.077	0.080	0.232	APT
Q5-4	0.003	0.035	0.214	–	–	0.031	0.073	0.283	APT
Q5-5	0.005	0.040	0.168	–	–	0.083	0.092	0.296	APT

Q5-Ave	0.003 ± 0.001	0.027 ± 0.013	0.191 ± 0.041	–	–	0.064 ± 0.020	0.079 ± 0.008	0.283 ± 0.039	

*Sum of Er, Sc, Zr and Group 5 elements.

In the present study, we arc-melted two alloys with the target composition Al-0.005Er-0.02Sc-0.07Zr-0.06Si at.%, with additions of 0.08 at.% Nb (labeled Q4) or 0.08 at.% Ta (labeled Q5), matching those of Q1 (unmodified) and Q2 (with 0.08 at.% V additions) in our previous study [36]: all compositions are given in Table 1. Due to its very high cost, the amount of Sc is minimized. A recently published study [36] shows that higher amounts of Sc (by a factor of 2.5 as compared to the present alloy) did not result in significant improvements in creep resistance to justify the cost. The alloys were homogenized and subjected to a double isothermal aging treatment, while measuring micro-hardness to assess peak strengthening and coarsening resistance; overaged samples were analyzed utilizing APT to assess the extent of Nb and Ta partitioning to the nanoprecipitates.

2. Experimental Procedure

Two 10 g buttons (Q4 with Nb additions and Q5 with Ta additions) were arc-melted (flipped and re-melted five times) in a water-cooled copper hearth furnace, using 99.99 at.% pure Al, 99.9 at.% pure Nb, 99.9 at.% pure Ta, and master alloys consisting of Al–5.9 wt% Er, Al–2 wt% Sc, Al–8 wt% Zr, and Al–12.6 wt% Si. Each button was sectioned into 2 mm thick specimens using an abrasive blade. One 2 mm thick slice per alloy was chemically analyzed using direct current plasma-atomic emission spectrometry (DCP-AES). The remaining sections were subjected to a homogenization treatment at 640 °C for 4 h (the same conditions as alloys Q1 and Q2 [36]) and a subsequent double-aging treatment at 350 °C/16 h and (400 or 450 °C)/12–720 h. The microhardness of all mounted and polished specimens was measured as the average of at least ten indentations, using a Duramin 5 microhardness tester (Struers) employing a 200 g load and a 5 s indentation time. Specimens double-aged at 350 °C/16 h + 450 °C/200 h were analyzed using a LEAP4000X Si tomograph (Cameca, Madison, WI) at a pulse repetition rate of 250–500 kHz, an ultraviolet (UV) (wavelength = 355 nm) pulse energy of 50 pJ, and a sample temperature of −243 °C (30 K). The three-dimensional (3-D) tomographic data were subsequently analyzed utilizing Cameca's integrated visualization and analysis software (IVAS), version 3.6.8. APT specimens were prepared by cutting blanks with a diamond saw to ~0.5 × 0.5 × 10 mm^3 and then subsequently electropolishing in two stages: (i) coarse electropolishing at 20–25 Vdc using a solution of 10 vol% perchloric acid in acetic acid to form a neck; and (ii) fine polishing at 15–18 Vdc using a solution of 2 vol% perchloric acid in butoxyethanol to dissolve the neck and obtain a nanotip [40,41].

3. Results and Discussion

Scanning electron microscope (SEM) micrographs of polished cross-sections of the as-cast alloys displayed a very small number of Zr-rich particles (one example from alloy Q4 is shown in Fig. 1), about 5 µm in size, formed during solidification, which are most likely primary Al_3Zr precipitates. In similar alloy systems, Er- and/or Zr-rich precipitates tend to form during solidification [34,35], and Er-rich precipitates dissolve during homogenization, while Zr-rich precipitates do not. This decreases the amount of Zr in solid-solution, which is available for subsequent precipitation during aging (thus decreasing the peak microhardness), and/or refines the grain structure, thereby decreasing the creep resistance. In our case it is, however, safe to assume that most of the alloying elements remain in solid-solution and are available to precipitate during aging, since the number density of primary precipitates is small. Our alloys also exhibit a dendritic microstructure, as anticipated based on prior studies [42,43]. All alloys are subjected to a homogenizing treatment at 640 °C for 4 h. This treatment dissolves primary Al_3Er and Al_3Sc (if present) precipitates. It doesn't, however, remove the interdendritic microstructure, particularly for the slow diffusers, which are Zr, Nb, and Ta. DCP-AES results display some discrepancies between the actual composition and the target compositions of both alloys. The Q4 and Q5 alloys

have verified compositions listed in Table 1. The Sc, Nb and Ta concentrations in alloys Q4 and Q5 are depleted by 35 to 50%, whereas the Er, Zr and Si concentrations are close to the target values.

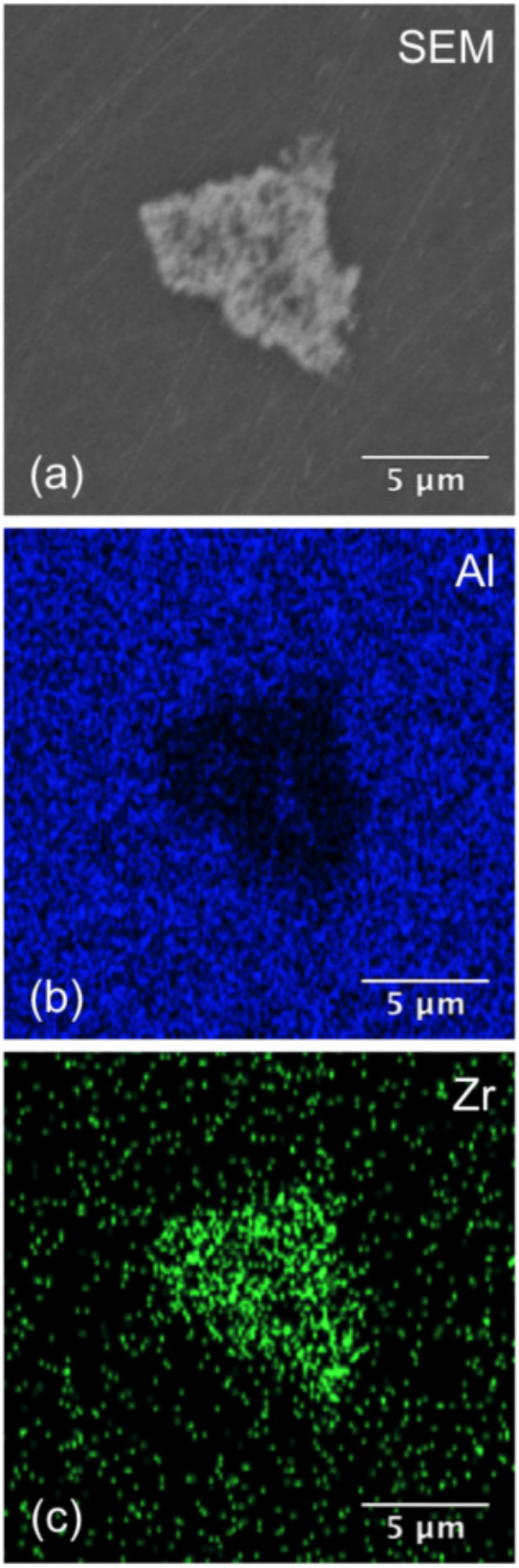

Fig. 1. (a) Scanning electron microscopy (SEM) image showing a primary Al_3Zr precipitate in the as-cast alloy Q4. Energy dispersive X-ray spectroscopy (EDS) maps displaying the distributions of (b) Al and (c) Zr.

The goal of the double-aging treatment is to maximize the number density of nanoprecipitates at the lower aging temperature (350 °C) and then permit the slow-diffusing elements, Zr, Nb or Ta, to precipitate at a higher temperature (400 or 450 °C) [36]. Employing an isothermal aging treatment at a single high-temperature (400 or 450 °C) is not ideal as nanoprecipitates consisting of the faster diffusing elements Er and Sc, would nucleate, grow, and coarsen rapidly before the slow-diffusing elements, particularly Zr, can form a shell around these nanoprecipitates to decelerate their coarsening kinetics. This would result in a small number density of nanoprecipitates and lower microhardness values and creep resistance. Alternatively, a single heat treatment at a lower temperature, while ensuring the formation of Er- and Sc-rich nanoprecipitates at a high number density, would not permit the slow-diffusing elements to precipitate from the solid-solution, at least for times relevant to industrial heat-treatments (a few days) or basic research (a few months).

Fig. 2 displays the evolution of the microhardness in alloys Q4 and Q5 during the second-step of the double-aging treatment, performed at 400 or 450 °C. Also presented for comparative purposes are the microhardness values for the two alloys, Q1 (no additions) and Q2 (with V-additions), previously published [36]. The Q1 and Q2 alloys were solidified in graphite molds placed on ice-cooled copper platens and quenched into water after solidification [36]. They may therefore be less supersaturated than the present arc-melted alloys Q4 and Q5 in the as-cast state; all alloys were homogenized (640 °C/4 h) prior to aging. The difference between the dendrite sizes may have an effect on the reported microhardness values. At 400 °C (Fig. 2(a)), for 12 to 120 h of aging, alloys Q2, Q4 and Q5 display a constant microhardness of 58–60 HV (~575 MPa), derived from the initial aging treatments at 350 °C. For these aging times, all values are within error bars, but alloy Q5 displays a slightly higher average microhardness. Beyond 200 h, the microhardness of alloy Q2 decreases significantly, whereas alloys Q4 and Q5 display only a very small decrease in microhardness values up to 720 h, for the longest aging time employed. The unmodified control alloy Q1 softens rapidly upon aging at 400 or 450 °C, and it displays a microhardness value significantly lower than alloy Q5 (425 vs 540 MPa) after 720 h, which is the longest aging time at 400 °C. This result is consistent with the absence of a slow-diffusing Group 5 element in this alloy. As displayed in Table 1, alloys Q4 and Q5 have smaller Sc concentrations than the V-containing alloy Q2, and smaller concentrations of $L1_2$ formers, which is the sum of Er, Sc, Zr and a Group 5 element; they, however, have a somewhat better coarsening resistance, especially at 400 °C. Increasing the Sc concentrations of alloys Q4 and Q5 to the same level as alloy Q2 alloy may further increase the strength of alloys Q4 and Q5, as Sc (unlike Zr and the Group 5 elements) precipitates strongly from a solid-solution. At 450 °C (Fig. 2(b)), all modified alloys are within a single band of data points, which decrease immediately upon aging. Based on previous results obtained from similar alloys [[34], [35], [36], [37]], including alloy Q2 discussed in this article, it is safe to hypothesize that the continuous decrease in microhardness in all alloys is due to the coarsening of $L1_2$ ordered nano-precipitates. The unmodified Q1 alloy is mechanically weaker than the modified alloys, but the difference with the modified alloys is less than at 400 °C. At all aging times, the alloy Q5 is stronger than alloy Q1 (380 MPa vs 350 after 720 h), while alloys Q2 and Q4 are intermediate in microhardness and very close to each other. The data show that the Sc concentrations in these alloys can be decreased from 0.013 at.% (Q2) to 0.007–0.009 at.% (Q4 and Q5), a factor of almost 2, without a reduction in coarsening resistance, making these alloys significantly less expensive. Alloys Q4 and Q5 must be retested after being conventionally cast, as alloys Q1 and Q2 were, to eliminate completely the possibility that differences in aging responses may be due to differences in the dendritic cast structures or to a higher supersaturation; the latter being unlikely, given the same homogenization conditions utilized.

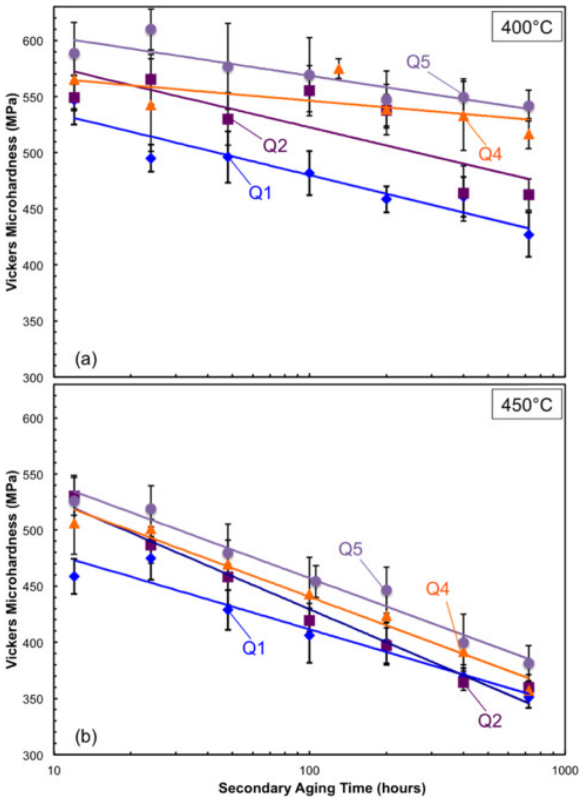

Fig. 2. Vickers microhardness (MPa) plots versus secondary aging time (hours) displaying its evolution for alloys Q1 (unmodified), Q2 (V-modified), Q4 (Nb-modified), and Q5 (Ta-modified) during double-aging with a primary step at 350 °C for 16 h, followed by secondary steps at: (a) 400 °C; and (b) 450 °C for times between 12 and 720 h.

An APT study was performed on alloys Q4 and Q5, which were double-aged at 350 °C/16 h plus 450 °C/200 h. The long aging time, 200 h, was chosen as a compromise between excessive coarsening (observed in Fig. 2 by the microhardness decrease) and insufficient diffusion of Nb and Ta. The proximity histogram [44] displayed in Fig. 3 shows the elemental concentration distributions in the matrix and nanoprecipitates, obtained from two partial nanoprecipitates, for alloy Q4. An increased Nb concentration is detected in the outer shell of the nanoprecipitate, near the interface with the matrix, indicated by a vertical dashed line, with a peak value of ~1.2 at.% or ~8 times the matrix's Nb concentration. This suggests that Nb partitions to the tri-aluminide nanoprecipitates and is consistent with the improved coarsening resistance when compared to unmodified alloy Q1. Also visible from this proximity histogram is the uniform concentrations of Er, Sc, and Zr within the nanoprecipitates. In similar alloy systems, including alloy Q2, a core-shell nanoprecipitate microstructure is observed, where an Er- and Sc-rich core is surrounded by a Zr-rich shell. Specifically, for alloy Q4 aged for 200 h (compared to 24 h for alloy Q2) the Zr-rich shell is also enriched in Nb, whose concentration reaches locally 0.3 at.%. Table 2 displays the matrix's and nanoprecipitates' average concentrations as determined by APT. It is evident that this particular nanotip is enriched in Zr and Nb, by factors of ~3.5 and ~4, respectively, as compared to the average values obtained utilizing DCP-AES. This indicates that this particular nanotip was most likely located in a dendritic core, as the peritectic-forming elements Zr and Nb are anticipated to segregate at the dendrite cores, whereas the eutectic-forming elements Er and Sc segregate in the inter-dendritic channels. The Zr concentration is higher than the average concentration measured using DCP-AES which supports the assumption that the nanotip volume sampled corresponds to the dendritic core. The compositional data also demonstrate that most of the Er, Sc, and Zr partitioned to the nanoprecipitates, as anticipated from prior studies [36,45]. While there is a significant amount of Nb partitioning to the nanoprecipitates, most of the Nb remains in

the matrix. The nanotip volume displayed in Fig. 3 contains 0.16 at.% Nb, which is almost four times the solid-solubility limit reported for the Al-Nb system at 450 °C (0.045 at.%), which can provide solid-solution strengthening [46].

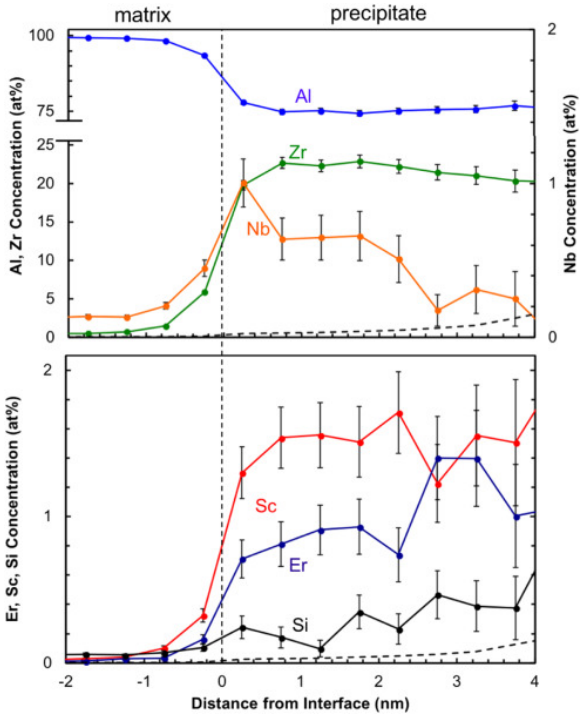

Fig. 3. Proximity histograms of two partial nanoprecipitates in alloy Q4-1 in the double-aged condition (350 °C/16 h plus 450 °C/200 h), indicating Nb partitioning to the nanoprecipitates. The vertical dashed line indicates the position of the matrix/nanoprecipitate interface. It is defined by the inflection point in the Al concentration profile. Dashed curves in both proximity histograms show the detection limit (plotted on the right ordinate), which represents a single ion detected in a bin.

Table 2. Matrix and precipitate concentrations (at.%) for alloys Q4 and Q5 nanotips analyzed utilizing atom-probe tomography (APT), for nanotips listed in Table 1, which contain nanoprecipitates. Data obtained from volumes with partial nanoprecipitates are less accurate than those with full nanoprecipitates (ND = not detected).

	Volume	**Er**	**Sc**	**Zr**	**Nb**	**Ta**	**Si**	**$L1_2$ Formers***	**Tip volume (nm^3)**	**Number of precipitates**
Q4-1	Matrix Precipitate	ND 0.96	0.002 1.54	0.131 24.84	0.157 0.26	– –	0.118 0.17	0.290 27.60	3×10^5	2 partial
Q4-2	Matrix Precipitate	0.005 0.16	0.005 1.43	0.225 21.14	0.024 0.01	– –	0.053 0.06	0.259 22.74	1×10^5	1 partial
Q4-6	Matrix Precipitate	ND ND	0.002 1.12	0.093 23.58	0.019 0.3	– –	0.075 0.14	0.134 25.0	2×10^6	2 partial
Q4-7	Matrix Precipitate	ND 0.29	0.008 8.65	0.104 16.24	0.210 0.24	– –	0.139 0.12	0.322 25.42	4×10^5	1 partial
Q5-1	Matrix Precipitate	0.002 0.76	0.016 4.84	0.216 18.21	– –	0.063 0.10	0.073 0.12	0.297 23.33	2×10^5	1 full
Q5-4	Matrix Precipitate	0.002 0.49	0.024 6.19	0.184 16.85	– –	0.031 ND	0.073 0.05	0.238 23.66	3×10^5	1 partial

Q5-5	Matrix Precipitate	0.001 1.15	0.009 9.97	0.130 12.54	– –	0.083 0.13	0.091 0.36	0.223 23.79	8×10^5	2 partial

Fig. 4 displays a proximity histogram obtained from alloy Q5, containing one full-nanoprecipitate, which exhibits an increase in Ta concentration as compared to the matrix composition (by a factor 1.6, Table 2), without localized interfacial segregation. This result indicates that Ta, like Nb in alloy Q4 (Fig. 3) and V in alloy Q2 [36], partitions to the tri-aluminide nanoprecipitates, consistent with enhanced coarsening resistance, Fig. 2. Unlike Nb and V, Ta (Fig. 4) is not segregated at the heterophase interface, but rather is present throughout the nanoprecipitates. Further comparisons between the APT results for these three alloys are difficult, as the analyzed volumes are depleted and enriched with alloying elements differently, due to dendritic segregation. The absolute concentrations of Group 5 elements in the nanoprecipitates may vary from nanotip-to-nanotip. Thus, comparing the matrix/nanoprecipitate partitioning coefficients, ratio of the concentration in a nanoprecipitate to that of the matrix, for the respective Group 5 elements is more informative. For alloys Q2 [36], Q4 (Fig. 3) and Q5 (Fig. 4), the partitioning coefficients are 2 for V, 1.6 for Nb and 1.6 for Ta, respectively. This indicates that the three Group 5 elements (V, Nb, and Ta) have approximately similar partitioning behaviors; their effects on the matrix/nanoprecipitate lattice parameter mismatch, affecting creep resistance, may be different as are their diffusivities in the aluminum matrix, which affects the coarsening resistance of the nanoprecipitates. The results presented herein reveal that Ta additions result in stronger and more coarsening resistant alloys; additional research, especially based on TEM imaging, is required, however, to definitely establish this point.

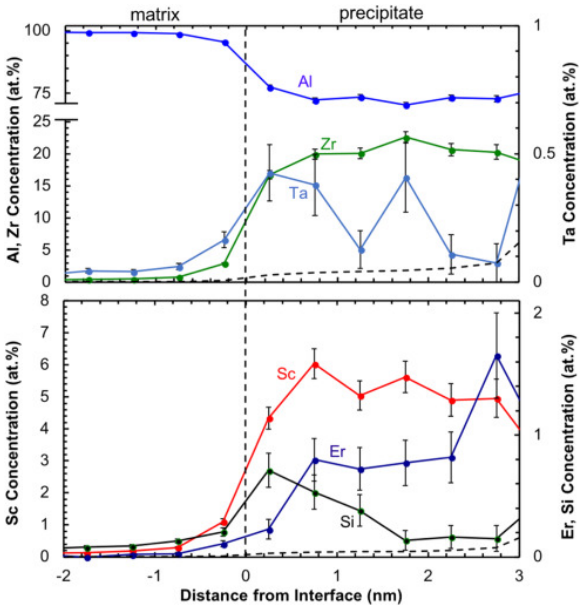

Fig. 4. Proximity histograms of one full nanoprecipitate in alloy Q5-1 in the double-aged condition (350 °C/16 h plus 450 °C/200 h), showing Ta partitioning to the nanoprecipitate. The vertical dashed-line indicates the position of the matrix/nanoprecipitate interface. It is defined by the inflection point in the Al concentration profile. Dashed curves in both proximity histograms show the detection limit (plotted on the right ordinate), which represents a single ion detected in a bin.

Due to the small number density of nanoprecipitates, there were at most two nanoprecipitates present in each of the nanotips analyzed. Although more nanotips were analyzed (listed in Table 1, Table 2), only one full nanoprecipitate was detected in the small volumes (listed in Table 2), which is consistent with a significant amount of coarsening at 450 °C. Thus, statistically-relevant values for the mean nanoprecipitate radius, volume

fraction and number density are not reported. Based on the nanotips analyzed, we expect the mean nanoprecipitate radius to be ~8 nm and the number density to be approximately 10^{21} m^{-3}, which is close to the values obtained for alloy Q2 (6 nm and 6.8×10^{-21} m^{-3}, respectively). Table 1 also displays the compositional variations among nanotips, which is a direct effect of the dendritic microstructure and elemental macro-segregation. The Er and Sc concentrations are anticipated to be under-determined, due to the lack of full nanoprecipitates in the volumes analyzed because these elements tend to partition to the nanoprecipitates's cores. The analyzed volumes must include multiple full nanoprecipitates for accurate results. Also, it is noted that, due to dendritic macro-segregation, the composition of one nanotip to another can vary significantly (as indicated by the relatively large error values given in Table 1). Hence, it is difficult to draw further conclusions without analyzing a larger number of nanotips, which is expensive.

4. Conclusions

The effects of Nb and Ta on the microstructural and microhardness evolution of arc-melted Al-Er-Sc-Zr-Si alloys are investigated. The following conclusions are reached as a result of this study:

1. As-cast alloys contain a small number density of Zr-rich primary precipitates, which were previously observed in similar alloys, but they do not have any significant negative effects on the alloys.
2. Double-aging studies are performed at a primary aging treatment at 350 °C for 16 h, which is followed by a secondary aging treatment at 400 or 450 °C for times up to 720 h. Both the Nb- and Ta-containing alloys (Q4 and Q5) displayed improved coarsening resistance at 400 °C compared to the base alloy Q1 and V-modified alloy Q2. This effect is not as significant at 450 °C. Alloys Q4 and Q5 are, however, still considerably stronger than alloys Q1 and Q2.
3. Atom-probe tomography results reveal increased concentrations of Nb and Ta at the matrix/nanoprecipitate heterophase interface in over-aged (350 °C/16 h plus 450 °C/200 h) alloys Q4 and Q5, respectively. This is similar to our prior results obtained from alloy Q2, where an increased V concentration at the matrix/nanoprecipitate heterophase interface was observed.
4. Due to the small number of nanoprecipitates observed in the analyzed atom-probe tomographic volumes, no definitive conclusions could be reached regarding the number density and volume fraction of said nanoprecipitates.

Acknowledgements

This publication was made possible by a National Priorities Research Program grant (NPRP 7-756-2-284) from the Qatar National Research Fund (a member of The Qatar Foundation). The statements made herein are solely the responsibility of the authors. ADL acknowledges some funding by the Ford-Northwestern University Alliance. The authors thank Profs. Ibrahim Karaman (Texas A&M University), Bilal Mansoor (Texas A&M University at Qatar), Georges Ayoub (University of Michigan-Dearborn), and Dr. Keith Knipling (Naval Research Labs) for useful discussions. Atom-probe tomography was performed at the Northwestern University Center for Atom-Probe Tomography (NUCAPT). The LEAP tomography system was purchased and upgraded with funding from NSF-MRI (DMR-0420532) and ONR-DURIP (N00014-0400798, N00014-0610539 and N00014-0910781) grants. Special thanks are extended to Drs. Dieter Isheim and Sung-Il Baik (NUCAPT) for their assistance with APT. DNS and DCD disclose that they have a financial interest in NanoAl LLC, which works in the area of aluminum alloys.

References

[1] E.A. Marquis, D.N. Seidman Acta Mater., 49 (2001), pp. 1909-1919
[2] D.N. Seidman, E.A. Marquis, D.C. Dunand Acta Mater., 50 (2002), pp. 4021-4035
[3] Z.M. Yin, Q.L. Pan, Y.H. Zhang, F. Jiang Mater. Sci. Eng. A, 280 (2000), pp. 151-155
[4] J. Royset, N. Ryum Int. Mater. Rev., 50 (2005), pp. 19-44
[5] J.Y. Zhang, X.Y. Jiang, M.Y. Ma, B. Jiang, B. Wang, D.Q. Yi Mater. Sci. Eng. A, 699 (2017), pp. 194-200

[6] O.N. Senkov, M.R. Shagiev, S.V. Senkova, D.B. Miracle Acta Mater., 56 (2008), pp. 3723-3738
[7] H. Wu, S.P. Wen, H. Huang, B.L. Li, X.L. Wu, K.Y. Gao, W. Wang, Z.R. Nie Mater. Sci. Eng. A, 689 (2017), pp. 313-322
[8] A. Tolley, V. Radmilovic, U. Dahmen Scr. Mater., 52 (2005), pp. 621-625
[9] S. Iwamura, Y. Miura Acta Mater., 52 (2004), pp. 591-600
[10] K.B. Hyde, A.F. Norman, P.B. Prangnell Acta Mater., 49 (2001), pp. 1327-1337
[11] K. Deane, S.L. Kampe, D. Swenson, P.G. Sanders Metall. Mater. Trans. A, 48A (2017), pp. 2030-2039
[12] R.A. Karnesky, D.N. Seidman, D.C. Dunand Mater. Sci. Forum, 519–521 (2006), pp. 1035-1040
[13] R.A. Karnesky, M.E. van Dalen, D.C. Dunand, D.N. Seidman Scr. Mater., 55 (2006), pp. 437-440
[14] Y. Harada, D.C. Dunand **Thermec 2006** Pts 1–5, 539–543 (2007), pp. 1565-1570
[15] R.A. Karnesky, D.C. Dunand, D.N. Seidman Acta Mater., 57 (2009), pp. 4022-4031
[16] M.E. van Dalen, R.A. Karnesky, J.R. Cabotaje, D.C. Dunand, D.N. Seidman Acta Mater., 57 (2009), pp. 4081-4089
[17] C. Booth-Morrison, D.N. Seidman, D.C. Dunand Acta Mater., 60 (2012), pp. 3643-3654
[18] Z.R. Nie, T.N. Jin, J.X. Zou, J.B. Fu, J.J. Yang, T.Y. Zuo Trans. Nonferrous Metals Soc. China, 13 (2003), pp. 509-514
[19] B. Gong, S.P. Wen, H. Huang, Z.R. Nie Acta Metall. Sin., 46 (2010), pp. 850-856
[20] H. Huang, S.P. Wen, K.Y. Gao, W. Wang, Z.R. Nie Metall. Mater. Trans. A, 44A (2013), pp. 2849-2856
[21] N.Q. Tuan, A.M.P. Pinto, H. Puga, L.A. Rocha, J. Barbosa Mater. Sci. Eng. A, 601 (2014), pp. 70-77
[22] Y. Harada, D.C. Dunand Acta Mater., 48 (2000), pp. 3477-3487
[23] Y. Harada, D.C. Dunand Mater. Sci. Eng. A, 329 (2002), pp. 686-695
[24] K.E. Knipling, D.C. Dunand, D.N. Seidman Zeitschrift Fur Metallkunde, 97 (2006), pp. 246-265
[25] S.K. Shaha, F. Czerwinski, W. Kasprzak, J. Friedman, D.L. Chen Mater. Sci. Eng. A, 652 (2016), pp. 353-364
[26] V.G. Davydov, V.I. Elagin, V.V. Zakharov, T.D. Rostova Met. Sci. Heat Treat., 38 (1996), pp. 347-352
[27] A.B. Spierings, K. Dawson, T. Heeling, P.J. Uggowitzer, R. Schaublin, F. Palm, K. Wegener Mater. Des., 115 (2017), pp. 52-63
[28] A.M. Samuel, S.A. Alkahtani, H.W. Doty, F.H. Samuel Mater. Des., 88 (2015), pp. 1134-1144
[29] C. Xu, W.L. Xiao, R.X. Zheng, S. Hanada, H. Yamagata, C.L. Ma Mater. Des., 88 (2015), pp. 485-492
[30] Y. Fan, M.M. Makhlouf J. Alloys Compd., 725 (2017), pp. 171-180
[31] C.B. Fuller, D.N. Seidman, D.C. Dunand Acta Mater., 51 (2003), pp. 4803-4814
[32] C.B. Fuller, J.L. Murray, D.N. Seidman Acta Mater., 53 (2005), pp. 5401-5413
[33] C.B. Fuller, D.N. Seidman Acta Mater., 53 (2005), pp. 5415-5428
[34] C. Booth-Morrison, D.C. Dunand, D.N. Seidman Acta Mater., 59 (2011), pp. 7029-7042
[35] C. Booth-Morrison, Z. Mao, M. Diaz, D.C. Dunand, C. Wolverton, D.N. Seidman Acta Mater., 60 (2012), pp. 4740-4752
[36] D. Erdeniz, W. Nasim, J. Malik, A.R. Yost, S. Park, A. De Luca, N.Q. Vo, I. Karaman, B. Mansoor, D.N. Seidman, D.C. Dunand Acta Mater., 124 (2017), pp. 501-512
[37] K.E. Knipling Microsc. Microanal., 22 (2016), pp. 688-689
[38] D.N. Seidman Annu. Rev. Mater. Res., 37 (2007), pp. 127-158
[39] D.N. Seidman, K. Stiller MRS Bull., 34 (2009), pp. 717-724
[40] B.W. Krakauer, J.G. Hu, S.M. Kuo, R.L. Mallick, A. Seki, D.N. Seidman, J.P. Baker, R.J. Loyd Rev. Sci. Instrum., 61 (1990), pp. 3390-3398
[41] B.W. Krakauer, D.N. Seidman Rev. Sci. Instrum., 63 (1992), pp. 4071-4079
[42] K.E. Knipling, D.C. Dunand Scr. Mater., 59 (2008), pp. 387-390
[43] K.E. Knipling, R.A. Karnesky, C.P. Lee, D.C. Dunand, D.N. Seidman Acta Mater., 58 (2010), pp. 5184-5195
[44] O.C. Hellman, J.A. Vandenbroucke, J. Rusing, D. Isheim, D.N. Seidman Microsc. Microanal., 6 (2000), pp. 437-444
[45] N.Q. Vo, D.C. Dunand, D.N. Seidman Acta Mater., 63 (2014), pp. 73-85
[46] R.P. Elliott, F.A. Shunk Bull. Alloy Phase Diagr., 2 (1981), pp. 75-81